Copyright

by

Eric Ou

2015

The Thesis Committee for Eric Ou
Certifies that this is the approved version of the following thesis:

Four-Probe Thermal Measurement of a Carbon Nanotube Sheet

APPROVED BY

SUPERVISING COMMITTEE:

Supervisor:

Li Shi

Yaguo Wang

Four-Probe Thermal Measurement of a Carbon Nanotube Sheet

by

Eric Ou, B.S.

Thesis

Presented to the Faculty of the Graduate School of

The University of Texas at Austin

in Partial Fulfillment

of the Requirements

for the Degree of

Master of Science in Engineering

The University of Texas at Austin

August 2015

Acknowledgements

Abstract

Four-Probe Thermal Measurement of a Carbon Nanotube Sheet

Eric Ou, M.S.E.

The University of Texas at Austin, 2015

Supervisor: Li Shi

As advances are made in top-down nanofabrication and bottom-up syntheses of nanostructures, the characteristic length scales encountered in these structures are on the order of the mean free path of the heat carriers or smaller. Therefore, the thermal transport properties of these nanostructures can be different from the bulk counterparts. A number of experimental techniques have been developed for characterizing the size-dependent thermal transport properties of nanostructures. However, it is difficult to eliminate contact thermal resistance, an important error source, from the measurement results. Recently, a four-probe thermal measurement technique has been developed to measure the intrinsic thermal conductance of a suspended sample as well as isolate the values of contact resistance between the sample and measurement device. Here, the fabrication process of the four-probe measurement device is described. In addition, numerical heat conduction simulation is used to verify the analytical model of the measurement method. This method is further used to measure the thermal conductance of a carbon nanotube sheet.

Table of Contents

List of Figures

Chapter 1: Introduction

Improvements in top-down nanofabrication and bottom-up syntheses of nanostructures have increased the demand for a better fundamental understanding of nanoscale materials and phenomena. The characteristic length scales of these materials and devices are on the order of the mean free paths of heat carriers or even smaller, where classical heat transfer laws are no longer applicable. Further advancements in nanotechnology will require a better scientific understanding of nanoscale thermal transport [1].

1.1 THERMAL TRANSPORT MEASUREMENT TECHNIQUES

The recent surge of interest in nanoscale thermal transport has motivated the development of a variety of thermal measurement devices and techniques for studying the thermal properties of nanoscale and two-dimensional (2D) materials. Some examples include time-domain thermoreflectance, bi-material cantilevers, Raman thermometry, and suspended resistance thermometer microdevices.

Time-domain thermoreflectance (TDTR) is a transient method that can be used to measure the thermal properties of thin films and interfaces [2, 3]. The samples are coated with a thin metal transducer layer [4] and then heated using an ultrafast laser. The transient temperature change of the metal transducer layer can be found by measuring the change in reflectance, which is a function of temperature. Because the reflectivity of the metal transducer depends on temperature, the transient reflectivity of the metal film measured by a probe beam can be used to obtain the transient temperature response, which can then be used to extract the thermal properties of the thin film sample. This technique has usually been used to measure the cross-plane thermal conductivity and interface thermal conductance in thin films. There have been recent developments of in-

plane thermal conductivity measurement using TDTR based methods, which is based on either offsetting the probe laser beam from the heating laser beam [5] or forming optical grating on the sample surface [6]. If the thin film sample is supported on a substrate, numerical heat conduction modeling is often required to estimate and eliminate the influence of the heat conduction in the substrate on the obtained in-plane thermal conductivity. If the thermal conductivity of the thin film is low compared to that of the substrate, it is difficult to measure the in-plane thermal conductivity of the supported thin film accurately. In addition, the lateral dimension of the sample needs to be considerably larger than the micron scale laser beam size, and the sample surface needs to be smooth for TDTR measurements. These requirements can limit the type of nanostructure samples that can be measured by TDTR.

Bi-material cantilever thermal sensors was used by Shen et al. to measure the axial thermal conductivity of polyethylene nanofibers [7]. In this measurement technique, a nanofiber sample is attached inline between a micro thermocouple and a reference bi-material cantilever. A laser is used to heat the tip of the reference cantilever, causing a measurable deflection in the cantilever tip due to the thermal expansion mismatch of the two constituent cantilever materials. By varying the laser power and the temperature of the thermocouple and measuring the deflection in the cantilever tip, the thermal conductance of the nanofiber was found. This method has only been used to measure compliant nanofibers; stiff fibers can affect the cantilever deflection.

Raman thermometry has been used to measure the thermal transport properties of suspended nanomaterials such as carbon nanotubes [8-10] and graphene [11-13]. This technique utilizes Raman scattering spectroscopy to probe the temperature of a sample while simultaneously heating the sample using either joule heating or laser heating. The temperature of a sample can be found by measuring the shift in certain Raman peaks or

from the intensity ratio of the Stokes and anti-Stokes Raman scattering signals [14]. By suspending the sample over a feature with known geometry, such as suspending a thin film sample over a circular hole, and simultaneously heating and measuring the temperature at the center of the sample, the thermal conductivity of the sample can be found by applying the heat equation to the system and solving with the measured temperature and known geometry. However, Raman thermometry typically suffers from limited temperature sensitivities. In addition, strain and other effects can also cause Raman peak shift. This effect can cause large errors in the obtained thermal transport properties.

Suspended resistance thermometer microdevices have been used to measure nanotubes and nanowires such as carbon nanotubes [15-17], silicon nanowires [18], and silicon-germanium nanowires [19, 20] as well as 2D layered materials such as graphene [21] and molybdenum disulfide [20]. The device is composed of a pair of platinum resistance thermometers, each patterned on a suspended silicon nitride (SiNx) membrane connected to the bulk substrate by long SiNx beams. These platinum resistance thermometers can act as resistive heaters and resistance thermometers. A sample is transferred onto the device so that it bridges the two membranes. One membrane is heated while both membrane temperatures are monitored using resistance thermometry. By measuring the temperature rise in the two membranes, the thermal resistances of both the sample and the supporting beams of each of the two membranes can be obtained.

1.2   MOTIVATION AND SCOPE OF THIS WORK

Although a number of experimental techniques have been developed for thermal transport measurements of nanostructures, an important challenge in many of these measurements is the difficulty to separate the contact thermal resistance from the intrinsic

thermal transport properties that need to be measured. Contact thermal resistance, or interfacial thermal resistance, causes finite temperature changes across material interfaces. These temperature drops are caused by imperfect contact at the material interface as well as scattering of energy carriers due to differences in the electronic and vibrational properties of materials.

To address this challenge, Kim *et al.* has recently developed a new four-probe thermal transport measurement method to isolate contact thermal resistance and measure the intrinsic thermal resistance of a nanostructured sample [23]. This work presents the device fabrication and numerical heat conduction analysis of the four-probe measurement device, and the application of this method for measuring the intrinsic thermal conductance of a carbon nanotube sheet.

Chapter 2: Development of a New Four-Probe Method

2.1 FOUR-PROBE THERMAL MEASUREMENT METHOD

The four-probe thermal measurement method uses four suspended patterned thin film metal resistance thermometer (RT) lines, across which a nanostructure sample is assembled as seen in Figure 2.1, to measure the intrinsic thermal conductance of the sample. During the measurement, one line is heated and the average temperature rises of all four RTs are obtained from the measured electrical resistances. This process is repeated until each of the four lines has been used as the heater line. The measurements obtain sixteen sets of measured average temperature rise data normalized by the electrical heating rate in the heating line i, $(IV)_i$, i = 1, 2, 3, 4. These data are used to obtain the thermal resistance ($R_{b,j}$, j = 1, 2, 3, 4) of each RT, the temperature rise ($\theta_{c,j,i}$) of the jth RT line at the contact point between the RT and the sample, and the heat flow rate ($Q_{j,i}$) across each contact point. The obtained results are used to find the intrinsic thermal resistance (R_2) of the sample as well as the values of the contact thermal resistance between the sample and the middle two RTs, $R_{c,2}$ and $R_{c,3}$. This measurement method is powerful since it has the ability to measure the intrinsic thermal resistance of a sample without errors from contact thermal resistance.
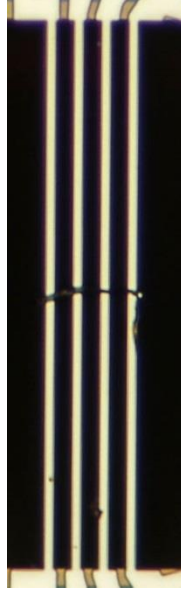
Figure 2.1: Optical micrograph of carbon nanotube sheet sample assembled on four-probe thermal measurement device

After obtaining the sixteen sets of average temperature rise data, the temperature distribution in each line is used to find the temperature at the contact point, $\theta_{c,j,i}$ [23]. For non-heated thermometer lines, the temperature distributions are linear and the temperature at the contact point is:

$$\theta_{c,j,i} = 2\bar{\theta}_{j,i}, \quad \text{for } j \neq i. \tag{2.1}$$

This contact point temperature is used to calculate the heat flow rate from each thermometer line into the nanostructure using the thermal resistance circuit shown in Figure 2.2. The heat flow rate for unheated and heated lines is:

$$Q_{j,i} = -\theta_{c,j,i}/R_{b,j}, \quad \text{for } j \neq i, \tag{2.2}$$

and

$$Q_{i,i} = -\sum_{j,j\neq i} Q_{j,i}. \tag{2.3}$$

The thermal resistance of each of the four thermometer lines is

$$R_{b,j} = \frac{L_j}{2k_j A_j}\left[1 - \left(\frac{d_j}{L_j}\right)^2\right], \tag{2.4}$$

where k_j, A_j, and $2L_j$ are the effective thermal conductivity, cross-sectional area, and length of the jth suspended thermometer line with deviation d_j from the center of the line to the contact point of the nanostructured sample.
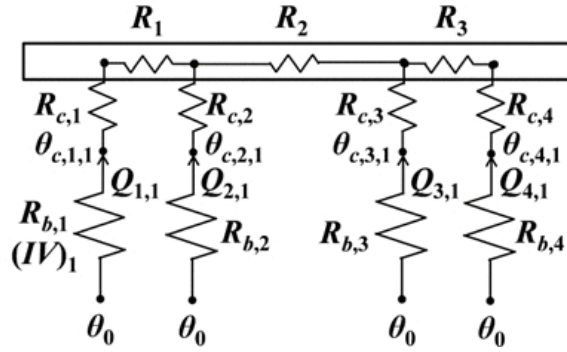
Figure 2.2: Thermal resistance circuit diagram representing the heat transfer in the four-probe thermal measurement device when the first line is heated ($i=1$) with Joule heating, $(IV)_1$. $R_{b,j}$ represents the thermal resistance of line j. $\theta_{c,j,i}$ is the temperature at the point of line j in contact with the sample when line i is heated. $Q_{j,i}$ is the heat flow in line j when line i is heated. $R_{c,j}$ is the contact resistance between line j and the sample. R_1, R_2, and R_3 are the thermal resistances of the left, middle, and right suspended sample segments [23].

To find the temperature distribution of the ith heated line, the heat conduction equation is applied with a heat flow boundary condition at the contact point with a magnitude of heating provided by Equation 2.3 which gives:

$$\theta_{i,i}(x) = \frac{(IV)_i}{4k_i A_i L_i}\left(L_i^2 - x^2\right) + \frac{\left[d_i + (-1)^{H(d_i-x)}L_i\right]}{2k_i A_i L_i}\left[x - (-1)^{H(d_i-x)}L_i\right]Q_{i,i} \tag{2.5}$$

where $H(\chi)$ is the Heaviside step function and x is the distance from the center of the thermometer line. This temperature distribution can be integrated over the entire length of the line to obtain the average temperature of the ith line:

$$\bar{\theta}_{i,i} = \frac{1}{2L_i}\int_{-L_i}^{L_i}\theta_{i,i}(x)dx. \tag{2.6}$$

After performing this integral for all four lines, the following relationship is obtained:

$$\sum_{j=1}^{4}\frac{\bar{\theta}_{j,i}/(IV)_i}{R_{b,j}} = \frac{1}{3[1-(d_i/L_i)^2]}, \quad \text{for } i = 1, 2, 3, \text{ and } 4, \tag{2.7}$$

which gives a set of four equations that can be written in matrix form and solved to yield the thermal resistances, R_b, of the four thermometer lines.

Using the thermal resistances of the thermometers lines, the contact point temperature rise for the ith heating line can be found using:

$$\theta_{c,i,i} = R_{b,i}\left[\frac{(IV)_i}{2} - 2\left(\sum_{j=1}^{4}\frac{\bar{\theta}_{j,i}}{R_{b,j}} - \frac{\bar{\theta}_{i,i}}{R_{b,i}}\right)\right] \tag{2.8}$$

Equations 2.1, 2.2, 2.3, and 2.8 can be used to find 16 pairs of $\theta_{c,j,i}/(IV)_i$ and $Q_{j,i}/(IV)_i$ data for i and j ranging from 1 to 4. These 16 pairs of data can be used to solve these sets of equations:

$$\theta_{c,2,i} - \theta_{c,3,i} = Q_{2,i}R_{c,2} + (Q_{1,i} - Q_{2,i})R_2 - Q_{3,i}R_{c,3}, \quad \text{for } i = 1,2,3,4, \tag{2.9}$$

$$\theta_{c,1,i} - \theta_{c,2,i} = Q_{1,i}(R_1 + R_{c,1}) - Q_{2,i}R_{c,2}, \quad \text{for } i = 1,2,3,4, \tag{2.10}$$

$$\theta_{c,4,i} - \theta_{c,3,i} = Q_{4,i}(R_3 + R_{c,4}) - Q_{3,i}R_{c,3}, \quad \text{for } i = 1,2,3,4, \tag{2.11}$$

which allows nine thermal resistances to be solved for, including the four beam resistances, $R_{b,1}$, $R_{b,2}$, $R_{b,3}$, and $R_{b,4}$, the intrinsic thermal resistance of the sample, R_2, two

contact resistances, $R_{c,2}$ and $R_{c,3}$, and two combinations of sample and contact resistances, $R_1 + R_{c,1}$ and $R_3 + R_{c,4}$.

2.2   DEVICE DEVELOPMENT

In order for the theory of the four-probe thermal measurement method to hold, several requirements must be fulfilled. The method requires four sets of four-probe metal resistance thermometer lines. These RTs need to be suspended to eliminate interface heat loss from these lines into the substrate. The temperature rise at the ends of the lines should be negligible, an assumption used to calculate the temperature profiles along the lines. The lines should also be thin enough so that the sample-RT interface can be approximated as a point contact, so that the temperature at either side of the contact is uniform even though there is a temperature difference across the contact.

The basic design of the four-probe thermal measurement device consists of four parallel, fully-suspended resistance thermometer lines that terminate into a high-thermal conductivity substrate. To achieve these basic requirements, the length of the RTs used in the four-probe thermal measurement devices are much longer than their width and thickness, allowing one-dimensional conduction analysis to be used for each RT line. The spreading thermal resistance of the substrate is two orders of magnitude smaller than the thermal resistance of the lines so temperature rise at the ends of the lines can be neglected.

In addition to these fundamental requirements for device operation, certain design considerations must be taken to facilitate device fabrication and use. For high device yield and throughput, the devices are fabricated using common photolithography and etching tools available at the Microelectronics Research Center.

One of the strict fabrication requirements for the devices is for them to not require any electron beam lithography. While electron beam lithography has the potential for far better resolution compared to traditional photolithography techniques, the throughput and availability of the equipment can greatly increase fabrication time and complexity. The photolithography tools available have a practical resolution limit of 1 μm which is adequate for these devices.

To accommodate different sample sizes, the width between any of the four RTs can be varied. To ensure an adequate temperature rise during the measurements, the thermal conductance of the lines should be roughly matched to the thermal conductance of the samples being measured. The length of the suspended thermometer lines can be used to change the thermal conductance without changing any other dimensions. Since the masks used during photolithography are custom fabricated, any design can be used, including different combinations of device geometries on the same mask.

One of the greatest challenges of nanoscale thermal measurements using micro-fabricated devices is the sample transfer process. In order to maximize the versatility of the devices, they should be compatible with as many sample transfer techniques as possible. Some samples can be transferred directly onto the devices using a micromanipulator and tungsten probe tip. The minimum line spacing used provides adequate room for handling the sample with the tungsten probe. Another sample transfer technique utilizes a polymer transfer layer, which is aligned on top of the devices. If a polymer transfer layer is used, it must be removed after the transfer by dissolving the polymer in an appropriate solvent or etchant. Alternatively, it can be burned off in a tube furnace. In order to be compatible with the high-temperature burning process, the devices must be able to withstand elevated temperatures for extended periods. Drop casting is another commonly used sample transfer technique in which the sample is dispersed in a

solvent and dropped directly onto the device. To increase the probability that a sample can land onto the thermometer lines, the number of lines per device can be increased to increase the density of measurement devices on a chip.

Once the samples are transferred onto the devices, the devices must be mounted and wire bonded to a chip carrier so that it can be used in a cryostat. The chip carrier determines the maximum size of an individual device chip. The devices need to have sixteen contact pads, four for each thermometer line. The contact pads must be large enough to be easily wire bonded and arranged in a way that will prevent the wires from crossing to prevent shorting.

Another design consideration that must be taken into account is material compatibility and suitability. The materials used should be compatible with the photoresist, solvents, and etchants used in the fabrication process. Metals used for the resistance thermometer lines should have a high resistance temperature coefficient that is linear for the desired temperature range of the measurement and should not be damaged by the temperatures used in the tube furnace for sample processing.

To fulfill these requirements, the devices are fabricated on 4" silicon wafers with SiN_x deposited on both sides. This wafer size was chosen to maximize throughput while maintaining compatibility with the majority of the equipment available. Palladium, chosen for its compatibility with metal lift-off and good resistance temperature coefficient, is used as the RT. All patterning on the wafers is done through photolithography. The completed device wafer is divided into device chips measuring 5mm x 6mm, the maximum practical size that can fit in the chip carrier, and contain nine devices each. A 4" wafer can accommodate 240 device chips for a maximum possible yield of 2160 devices.

2.3 DEVICE FABRICATION

The devices are fabricated on 4" silicon wafers with 300-500 nm of SiN_x deposited on the front and back. The wafers are first cleaned using Piranha solution, a mixture of sulfuric acid and hydrogen peroxide. Piranha solution removes organic matter and can also remove particles and other contaminants.

Once the wafers have been cleaned, the wafers are then put in an oven that dehydrates the wafers completely and deposits hexamethyldisilazne (HMDS), which acts as an adhesion promoter for photoresist. Photoresist is then spun onto the wafer proceeded by a pre-exposure or soft bake, evaporating any remaining solvent from the resist.

The metal used in the devices is patterned using a lift-off process where a sacrificial layer is first deposited and patterned in the inverse of the desired design. The target material is then deposited over the entire wafer; the desired target material is deposited directly onto the substrate, while the rest is deposited onto the sacrificial layer. The sacrificial layer can then be removed along with the undesired target material, leaving just the desired pattern.

In the first photolithography step, an image-reversal process is used to create an undercut profile, which creates a clean break in the deposited metal layer and facilitates lift-off. First, the inverse of the desired pattern is exposed to UV using a negative mask. The substrate and exposed photoresist are then baked, cross-linking the previously exposed photoresist and rendering it insoluble in developer. The previously unexposed area remains photoactive. The entire wafer is then flood exposed in UV light, making the previously unexposed area soluble in developer. After developing, the desired pattern with an undercut profile is obtained.

Metal is then deposited onto the wafers using an electron-beam evaporator, covering the entire surface of the wafer. For the devices, a 10 nm adhesion layer of chromium is deposited followed by 200 nm of palladium. The wafers are submerged in heated Remover PG, a solvent stripper, to remove the photoresist and lift-off the undesired metal. After the photoresist has been removed, the wafers are thoroughly cleaned to remove any remaining residues.

To create a fully suspended, etched-through device, the SiN_x on the front and back of the wafers must be patterned to expose the underlying silicon so that it can be etched. To selectively remove SiN_x from the wafers, photoresist is used as an etch mask during plasma etching with tetrafluoromethane (CF_4) gas. Since photoresist is only being used as an etch mask, the photoresist is exposed normally using a positive mask. After development, the wafers are not post-exposure baked since the unhardened photoresist is sufficiently thick enough to mask the rest of the wafer. Post-exposure baking the wafer can make the photoresist harder to remove in subsequent steps, leaving potential residues. The wafers are etched using a reactive-ion etcher with CF_4 gas until the exposed SiN_x layer is completely etched through. This process is repeated to pattern the backside of the wafer.

After windows have been etched in the SiN_x on both the front and back of the wafer, the silicon substrate between the two windows is etched completely using tetramethylammonium hydroxide (TMAH). The wafers are etched using a single-wafer wet-etching apparatus that allows the wafer to be etched from only one side. The wafers are etched starting from the backside until they are etched through.

2.4   FABRICATION CHALLENGES

Alignment of the two photolithography layers on the top of the wafer was one of the great challenges faced during the development of the devices. The first layer consists of eight long, narrow thermometer lines that terminate into contact pads. Since the desired line width of the thermometer lines, 1-2 μm, is comparable to the alignment accuracy of most mask alignment tools, it is possible to easily misalign the two layers, leaving the metal lines completely exposed while masking some of the nitride that should be etched during the second photolithography step.

One possible solution is to forgo masking the lines and exposing the entire window where SiN_x is to be etched, including the RTs. The metal lines can prevent the underlying nitride from being etched in this self-aligned process, guaranteeing that the SiN_x underneath follows the exact profile of the RTs. To protect the RTs from being etched by the plasma, two additional layers of metal are deposited, a sacrificial layer and a protective layer. Titanium was used as the sacrificial layer since it can be deposited with a large thickness and etched easily. Chromium was used as the protective layer for its resistance to CF_4 plasma.

The self-aligned process itself worked perfectly; however, removing the protective layer by etching the sacrificial layer proved to be very difficult. At the time, a positive photolithography process and lift-off was used to selectively deposit the metal layers. Due to the photoresist profile of the positive photolithography process, which can have sloping sidewalls that cause the metal to form a continuous layer, the metal layer did not lift-off cleanly. This issue combined with poor metal adhesion caused the resistive thermometer metal layer to be damaged while the sacrificial metal layer was being etched. Additionally, although the titanium sacrificial layer was thick compared to the

14

other metal layers, it was still very thin, preventing adequate etchant penetration and leading to long etching times.

To improve metal to SiN_x adhesion, the additive lift-off process was replaced by a subtractive dry etching process in which the metal layer is deposited on the wafer first and then photolithography and plasma etching is used to selectively remove metal. This process greatly complicates the device fabrication process since photoresist is not a suitable mask for the argon plasma required to etch the metal. To work around this limitation, a layer of silicon oxide is deposited on top of the metal layer as a masking layer. A photolithographic process using a negative mask is used to pattern the oxide layer. The photoresist acts as a mask for plasma etching silicon oxide in CF_4 plasma, which transfers the mask pattern to the oxide layer. The photoresist is then removed and the patterned oxide layer is used as a mask for the metal etch in argon plasma. The oxide can be etched afterwards using hydrofluoric acid (HF).

Although the metal etching process itself produced satisfactory results, the silicon oxide deposition process would leave hard to remove particles on the surface of the wafer, contaminating the devices. To prevent device contamination and simplify the device fabrication process, an image-reversal process was tested. Since the image-reversal process uses a negative mask to produce a positive image, the existing negative mask for the subtractive etching procedure could be used. Due to the undercut photoresist profile, the image-reversal process produced very good edge definition and resolution of the metal layer. Instead of using an addition protective layer, more metal is deposited during the evaporation process to compensate for thinning during the plasma etch. The image-reversal process offers the best combination of patterning quality and throughput and avoids the lengthy silicon oxide deposition process required for subtractive fabrication techniques.

15

Chapter 3: Numerical Modeling

Numerical modeling of the four-probe measurement devices can be used to check the validity of assumptions made during analysis as well as to improve the accuracy of the devices by tuning different geometric parameters to reduce errors.

3.1   GOVERNING EQUATIONS

Though microscale heat transfer effects may be important in some samples, the length scale of the device is large enough that heat transfer is governed by Fourier conduction. The measurement takes place under high vacuum so heat lost due to convection and air conduction is eliminated. Previous calculations have shown that heat lost due to radiation is several magnitudes lower than the heat conducted through the device so radiative heat transfer is also ignored [23].

Since both convection and radiation are ignored, the problem is governed strictly by 3-dimensional (3D) heat conduction given by Equation 3.1 [24]:

$$\boldsymbol{q} = -k\nabla T \tag{3.1}$$

A Dirichlet boundary condition is applied to the ends of the lines where they terminate into the bulk Si substrate. Since the temperature rise at the ends of the lines is negligible, the temperature at the boundary is assumed to be the substrate temperature, T_0. Because the problem only considers heat conduction, all exterior surfaces other than the ends of the lines are considered to be adiabatic.

3.2   NUMERICAL METHOD

The finite volume method is used to solve the temperature field in the lines and the sample [25]. A 3D structured mesh is used for simplicity. Figure 3.1 represents one control volume with lines connecting to neighboring control volumes in the positive and negative x, y, and z directions.
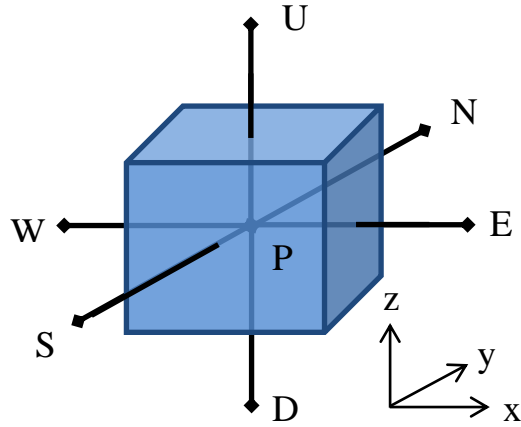
16

Figure 3.1: Representative control volume with cell centroid at Point P with six neighboring cells, Points U, N, E, S, W, and D.

The heat conduction equation can be written as:

$$\nabla \cdot \boldsymbol{q} = S \tag{3.2}$$

where S represents a heat generation source term. Equation 3.2 can be integrated over a control volume to yield:

$$\int_{\Delta V} \nabla \cdot \boldsymbol{q} \, dV = \int_{\Delta V} S \, dV \tag{3.3}$$

which can also be written as a summation:

$$\sum_{f} \boldsymbol{q}_f \cdot \boldsymbol{A}_f = \bar{S} \Delta V \tag{3.4}$$

where f represents the six faces bordering neighboring cells shown in the control volume in Figure 3.1 and $\bar{S}$ is volumetric heat generation. If the temperature T is assumed to vary linearly between cell centroids, then ∇T can be represented by the difference of temperatures at cell centroids divided by the distance between cell centroids and Equation 3.4 can be rewritten as:

$$a_p\varphi_p = a_E\varphi_E + a_S\varphi_S + a_W\varphi_W + a_N\varphi_N + a_D\varphi_D + a_U\varphi_U + b \tag{3.5}$$

where

$$a_P = a_E + a_S + a_W + a_N + a_D + a_U \tag{3.5a}$$

$$a_E = \frac{k\Delta y\Delta z}{(\delta x)_e} \tag{3.5b}$$

$$a_S = \frac{k\Delta x\Delta z}{(\delta y)_s} \tag{3.5c}$$

$$a_W = \frac{k\Delta y\Delta z}{(\delta x)_w} \tag{3.5d}$$

$$a_N = \frac{k\Delta x\Delta z}{(\delta y)_n} \tag{3.5e}$$

$$a_D = \frac{k\Delta x\Delta y}{(\delta z)_d} \tag{3.5f}$$

$$a_U = \frac{k\Delta x\Delta y}{(\delta z)_u} \tag{3.5g}$$

$$b = \bar{S}\Delta x\Delta y\Delta z \tag{3.5h}$$

Since the Pt and SiN$_x$ used in the device have different thermal properties, the discrete equation above must be modified in cells in contact with a different material. Figure 3.2 represents two adjacent unit cells of different materials. Here the temperature T is assumed to vary linearly between Point P and the face and between the face and Point U. The heat flow from Point P to Point U can be expressed as:

$$\boldsymbol{q}_u \cdot \boldsymbol{A}_u = \frac{T_P - T_U}{R_A + R_B} \tag{3.6}$$

where

$$R_A = \frac{(\delta z)_A}{k_A \Delta x \Delta y} \tag{3.6a}$$

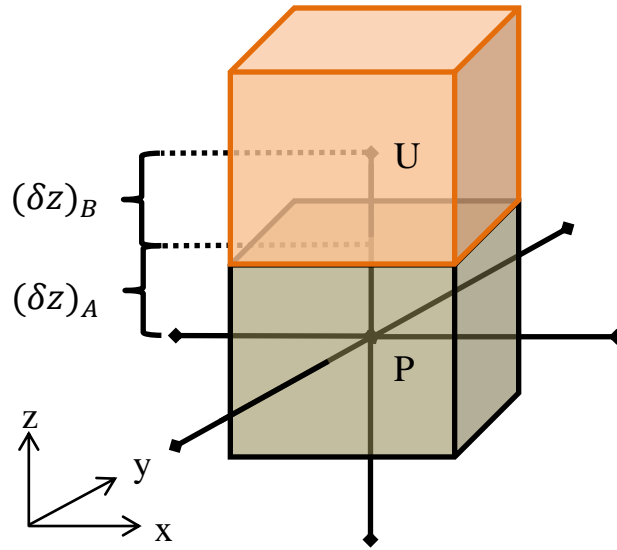$$R_B = \frac{(\delta z)_B}{k_B \Delta x \Delta y} \tag{3.6b}$$

Figure 3.2: Two adjacent unit cells representing different materials.

Contact thermal resistance between two surfaces leads to a finite temperature drop across an infinitesimally small distance. The heat transfer across an interface with contact resistance is:

$$\boldsymbol{q} \cdot \boldsymbol{A} = \frac{\Delta T}{R_c}$$

(3.7)

where R_c is thermal contact resistance. A thermal contact resistance term can be added to Equation 3.6 to incorporate contact resistance at the interface between two different materials:

$$\boldsymbol{q}_u \cdot \boldsymbol{A}_u = \frac{T_P - T_U}{R_A + R_c + R_B}$$

3.8)

To incorporate contact resistance into the discrete equation, the coefficient for the direction of the neighboring cell of dissimilar material is modified. If the lower cell in Figure 3.2 is material A and the cell above, material B, then the a_U coefficient is modified to include contact resistance:

19

$$a_U = \frac{1}{\frac{(\delta z)_A}{k_A \Delta x \Delta y} + R_{contact} + \frac{(\delta z)_B}{k_B \Delta x \Delta y}} \qquad (3.9)$$

Once the device and sample system has been discretized, the set of equations can be solved using a line-by-line tri-diagonal matrix algorithm (TDMA) or solved directly using matrix inversion. Both methods have been used to obtain the same results, given enough iterations of the line-by-line TDMA. With the mesh sizes used, the direct method yielded faster results without the need to check if the system has reached the steady state solution as is needed with an iterative method.

3.3   SIMULATION RESULTS

A structured, but variable mesh was used to represent the system. In the x direction (across the thermometer lines) the system was divided into 40 uniformly spaced divisions. Since the length of the lines is much longer than their width, three different mesh sizes were used in the y direction (along the thermometer lines) based on the position on the line. Smaller divisions were used close to the sample location for better resolution. In the z direction, three different mesh sizes were also used, one for each material. In the y and z directions, the system was split into 50 and 3 divisions respectively for a final mesh size of 40x50x3 or 6000 cells.

The parameters used in the simulation are similar to the geometries and material properties of the measurements reported by Kim *et al.* [23]. The simulated lines are 200 μm long and 1 μm wide. The spacing between the lines is 3 μm, 12 μm, and 3 μm for a total system width of 22 μm. The simulated sample has a square cross section of 250x250 nm and a thermal conductivity of 60 W/mK. The beam thermal resistance is 88 K/μW and the total resistive heating simulated is 1 μW. Figure 3.3 and Figure 3.4 show the temperature distributions of the four lines when line 1 is heated for low R_c, 0.1 K/μW,

and high R_c, 100 K/µW. The temperature distribution along the sample is presented in Figure 3.5 and Figure 3.6 for the cases when line 1 and line 2 are heated for low R_c and high R_c.
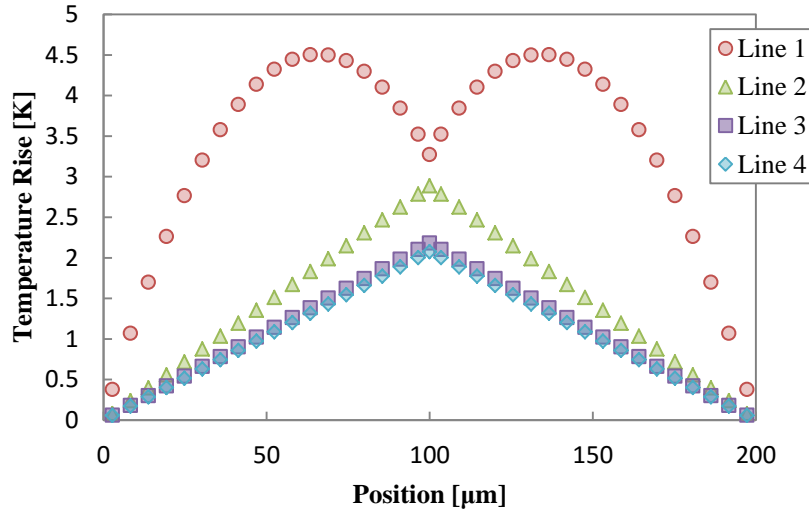

Figure 3.3: Temperature as a function of position along the thermometer lines when line 1 is heated and R_c is two orders of magnitude smaller than R_b.
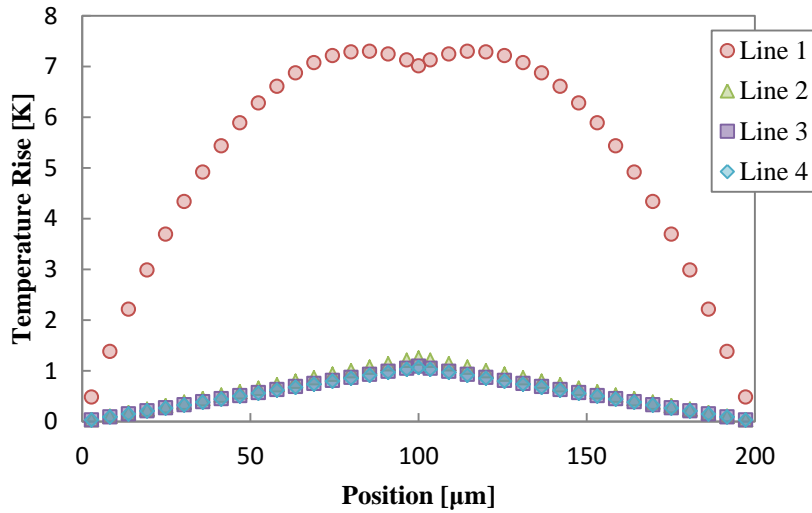

Figure 3.4: Temperature as a function of position along the thermometer lines when line 1 is heated and R_c is the same order of magnitude as R_b.
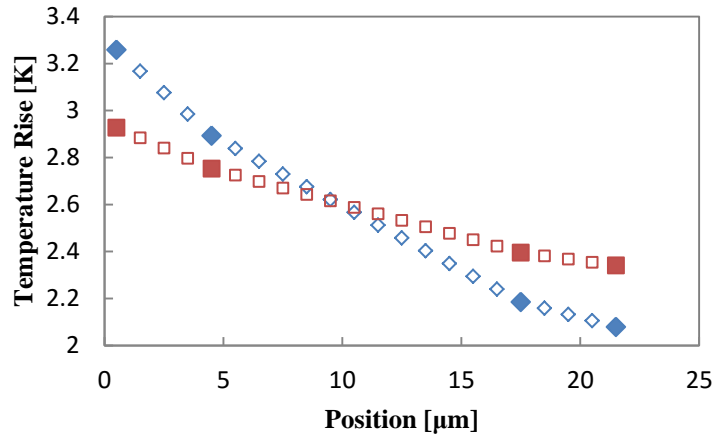
Figure 3.5: Temperature profile along sample for low R_c (diamonds) and high R_c (squares) when line 1 is heated. Filled markers denote where the sample is in contact with the lines.

Figure 3.6: Temperature profile along sample for low R_c (diamonds) and high R_c (squares) when line 2 is heated. Filled markers denote where the sample is in contact with the lines.

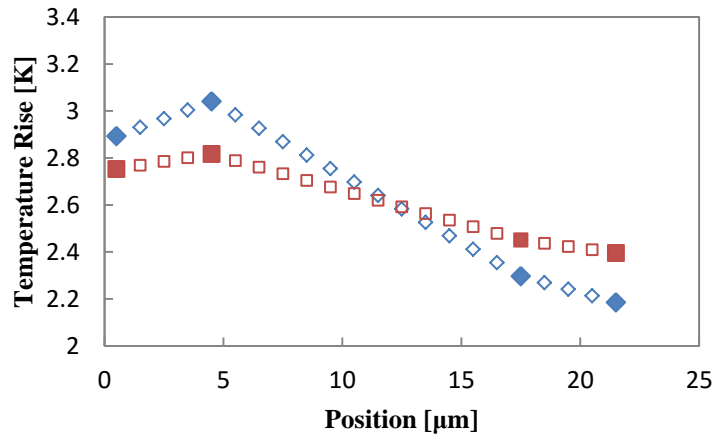The temperature distributions match expected values; the temperature distribution in the heated lines is parabolic in nature and linear in the unheated lines. When R_c is high, there is a large temperature drop between the lines and the sample. As a result, more heat

22

is transferred from the heated line into the substrate instead of flowing through the sample.

Using the data analysis for the measurement method, the correct intrinsic thermal conductivity of the sample was recovered within 1% and the R_c calculated was within one order of magnitude of the inputted value.

Based on the results of the model, the assumptions made during data analysis are mostly valid. However, the contact resistance, R_c, could not be successfully recovered for all device and sample geometries. The model can be used in future work to optimize the device and sample geometries used in order to increase measurement accuracy. The model can also be modified to account for sample offset from the center of the device.

Chapter 4: Nanotube Sheet Measurement

To demonstrate the effectiveness of the four-probe thermal measurement method, a carbon nanotube sheet, grown on ultrathin graphite foam, is assembled on a device and measured.

4.1 BACKGROUND AND STRUCTURAL PROPERTIES

While many nanomaterials exhibit extraordinary material properties on their own, they can also be used to augment the properties of bulk materials or even other nanomaterials by making composite and hybrid materials. Due to their unique combination of excellent mechanical, thermal, and electrical properties, which depend on their structure and diameter [26], carbon nanotubes are an ideal candidate as an advance filler material in nanocomposites [27]. Research has already shown the potential of carbon nanotubes for enhancing the mechanical and electrical properties of polymers [28-30] and even metals such aluminum [31, 32].

Theoretical work has predicted that the room temperature thermal conductivity of nanotubes is as high as 6600 W/mK [33] while measurements of single-walled carbon nanotubes have reported values as high as 3500 W/mK [17, 34, 35]. These high thermal conductivity values have naturally led to interest in carbon nanotubes for enhancing the thermal conductivity of composites for thermal management [36, 37] as well as enhancing the performance of thermal interface materials [38].

By growing carbon nanotubes on a graphite foam structure, it is possible to create a hybrid material with different properties and potentially better functional performance than the components individually. To gain more insight into the physics and component interactions in hybrid materials, it is important to study the individual components. Pettes *et al.* have investigated the effects of isotope impurity scattering on the thermal

conductivity of ultrathin graphite foams [39]. It is still necessary to investigate the thermal properties of the nanotubes grown directly on the foam, which can have different properties than nanotubes grown by other methods.

4.2 SAMPLE ASSEMBLY

The samples were prepared by sonicating a piece of the graphite/carbon nanotube foam in isopropyl alcohol. The dispersion was then drop-casted onto a silicon wafer piece. Samples were picked up from the wafer piece using a tungsten wire probe attached to a micromanipulator and transferred directly onto the measurement device as seen in the left panel of Figure 4.1. The device chip is then wire bonded to a chip carrier and loaded into a temperature controlled cryostat where measurements are done under vacuum to minimize the effects of convection. The cryostat stage also has a radiation shield to minimize radiation loss.
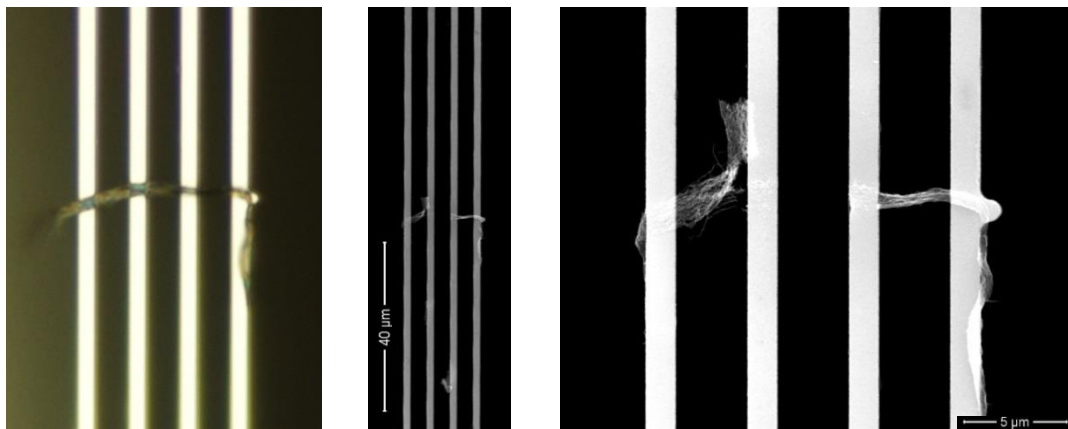

Figure 4.1: Optical micrograph (left panel) of carbon nanotube sheet sample as assembled on four-probe thermal measurement device. SEM images (center and right) of broken carbon nanotube sheet after measurement

4.3 MEASUREMENT METHOD AND RESULTS

As mentioned before, the four-probe thermal measurement method uses four sets of four-probe resistance thermometers, across which a sample is assembled. During the measurement, a DC current is supplied to one of the resistance thermometer lines to provide joule heating. The current is provided by applying a voltage across a high precision resistor with a low temperature coefficient of resistance, ensuring that the resistance stays constant throughout the measurement. The voltage drop across the resistor can be used to find the heating current. The voltage drop across the heated line is also measured so that the resistance of the thermometer line can be found. The electrical resistance change of the other thermometer lines is also measured using an electrical four-probe sensing method. Figure 4.2 shows the change in the resistance of the four thermometer lines as a function of heating current when the third line is heated.
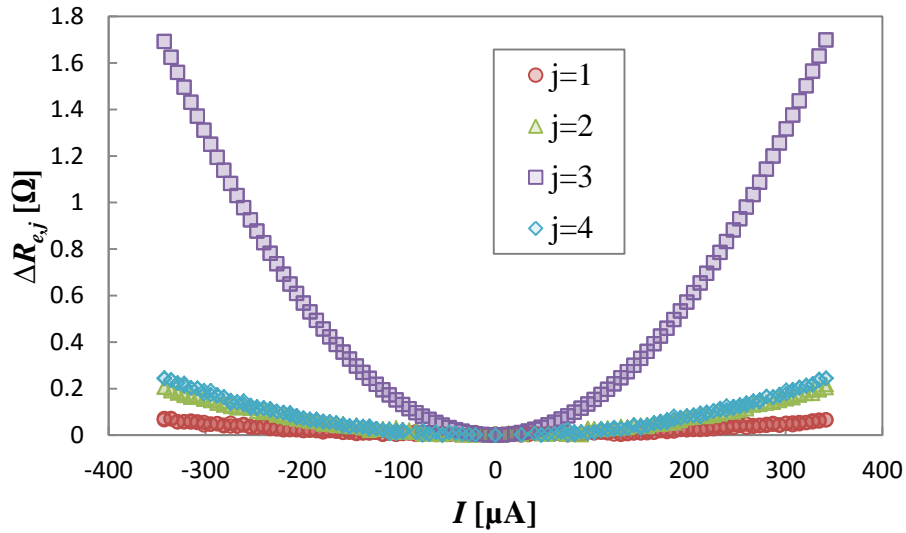

Figure 4.2: Change in electrical resistance as a function of DC heating current in Line 3 when sample stage temperature $T_0 = 250$K.

The electrical resistance of the metal used in the devices has a linear dependence on temperature in the temperature range used in the measurement. By measuring the electrical resistance of the lines when no heating is applied at different temperatures and assuming the lines are at the same temperature as the cryostat stage, a temperature dependence of electrical resistance can be found which allows changes in electrical resistance of the thermometer lines to be converted into the average temperature rise of the line. Figure 4.3 shows the electrical resistance of the thermometer lines when no heating is applied at different cryostat temperatures. The ratio of resistance change to temperature change, dR/dT, is found by taking the slope of the plot in Figure 4.3 and was found to be approximately 0.23 Ω/K. This value is used to convert resistance change to temperature rise which is plotted against electrical heating in Figure 4.4.
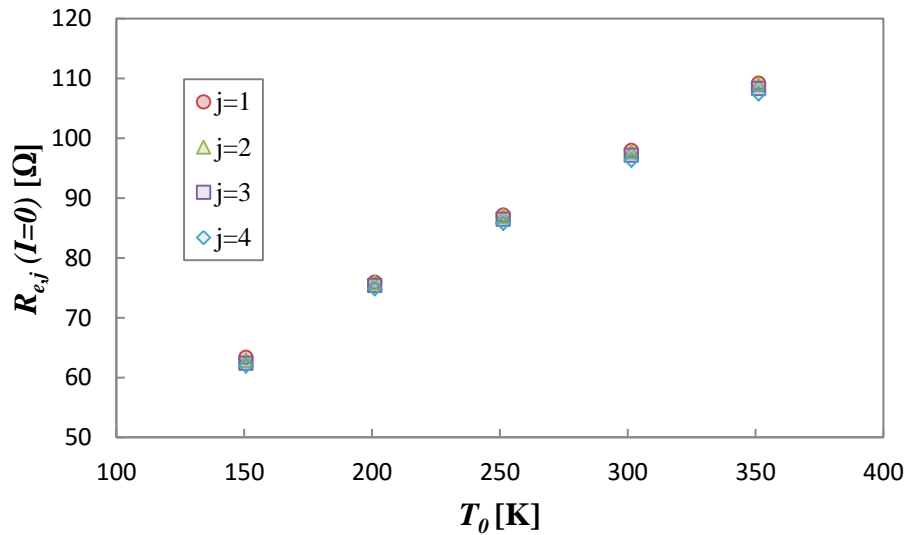

Figure 4.3: Changed in electrical resistance as a function of sample stage temperature (T_0) when no electrical heating is applied.
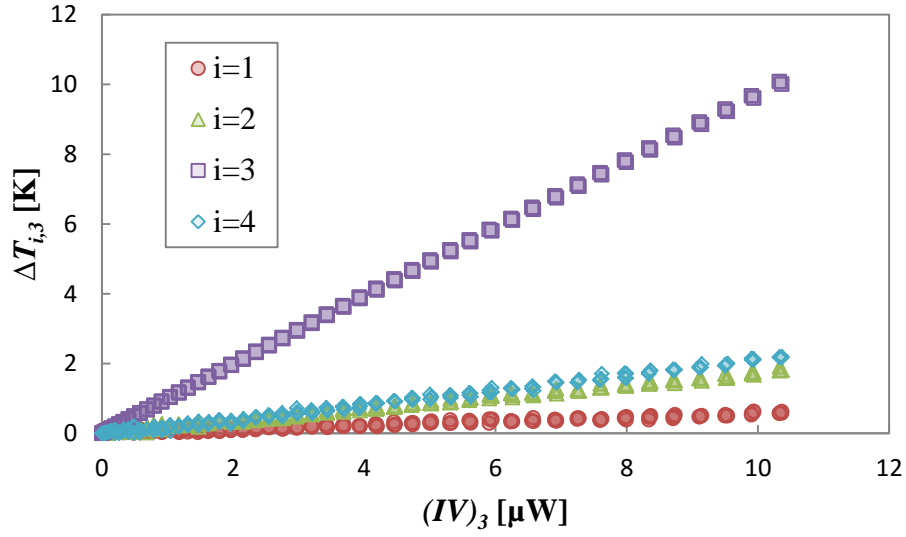
Figure 4.4: Average temperature rise as a function of the electrical heating in Line 3 at sample stage temperature $T_0 = 250$K.

The slope of the data presented in Figure 4.4 is used in Equation 2.7 to calculate the thermal resistances of the four thermometer lines, which is plotted as a function of sample stage temperature in Figure 4.5. The thermal resistances of the thermometer lines are then used to find the heat flow rates into the sample at the contact points which is shown Figure 4.6 as a function of heating line current. Once the contact point temperatures and heat flow rates have been calculated, the intrinsic thermal resistance of the sample can be found. Figure 4.7 presents the intrinsic thermal resistance of the carbon nanotube sheet along with values of the contact thermal resistance between the nanotube sheet and two different resistance thermometers.
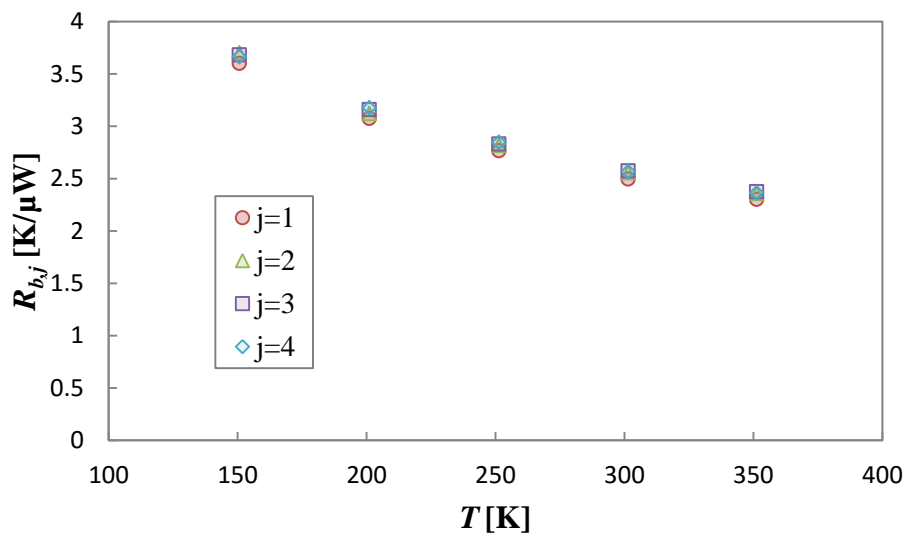
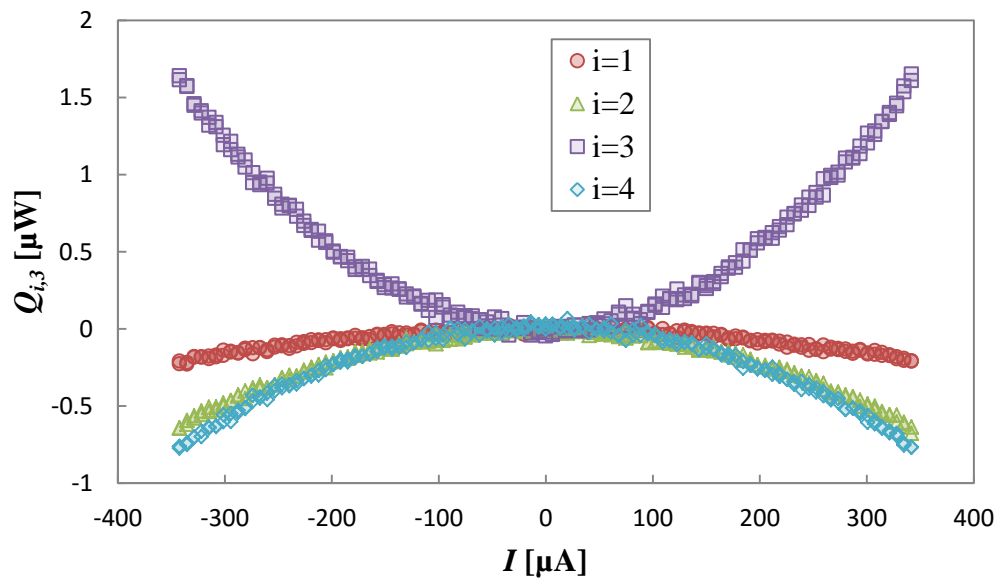Figure 4.5: Beam thermal resistance as a function of temperature

Figure 4.6: Net heat flow rate across the contact point from each RT into the sample as a function of the heating current in line 3 at 250K cryostat temperature
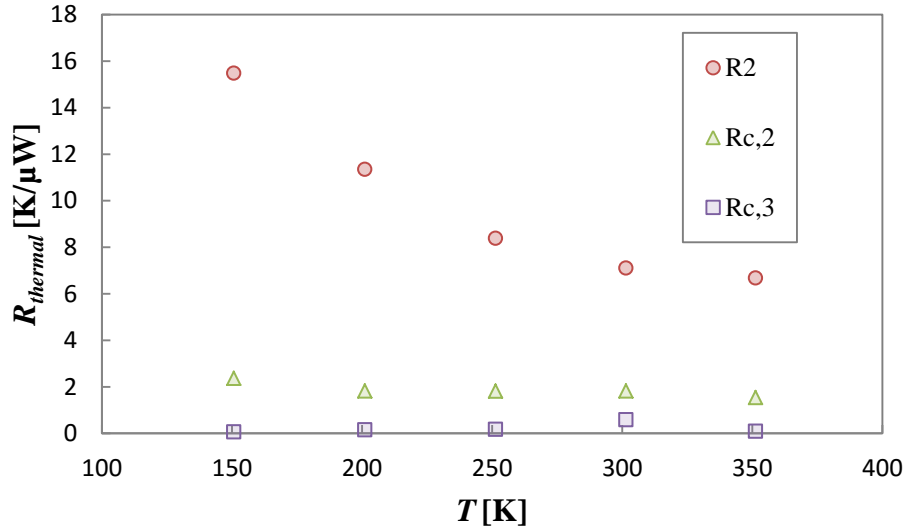
Figure 4.7: Thermal resistance as a function of temperature

In order to convert the measured thermal resistance into thermal conductivity, the cross section of the nanotube sheet needs to be obtained. However, it is found from scanning electron microscopy measurements that the sample cross section is rather irregular, and not well defined. Hence, only the thermal conductance of the center suspended section of the sample, shown in Figure 4.8, is reported. The obtained thermal conductance increases with temperature in the range between 150 and 350 K. In comparison, the thermal conductivity of long and defect-free individual nanotubes is expected to show a peak at low temperatures, above which the thermal conductivity decreases with increasing temperature because of increased phonon-phonon scattering. The different temperature dependence observed here suggests that phonon-phonon scattering is not dominant in the sample compared to scattering at contacts between nanotubes in the sheet.
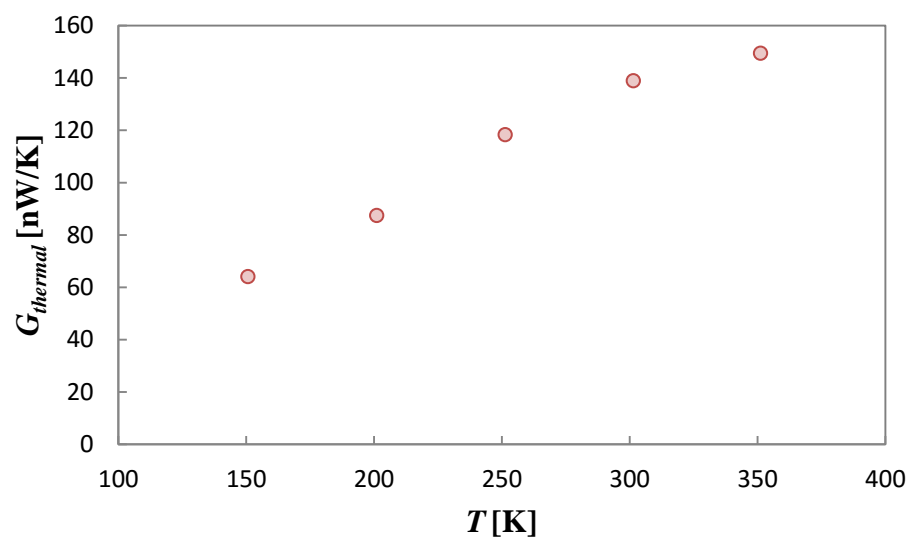
Figure 4.8: Thermal conductance as a function of temperature for carbon nanotube sheet
section suspended between the center two lines of the four-probe
measurement device

Chapter 5: Conclusion

This work has focused on the fabrication and numerical simulation of a newly developed micro-device for four-probe thermal transport measurement. The fabrication process and challenges are reported along with the framework for the numerical simulation of the measurement micro-device. Through careful design and selection of fabrication processes, the device yield can be maximized. Numerical simulation has been used to verify the analytical model of the measurement device. In order to show the effectiveness of this measurement method, a carbon nanotube sheet, grown from an ultrathin graphite film, is measured. The obtained thermal conductance of a 3.5 μm long suspended section is approximately 140 nW/K at room temperature. These results are useful for further development of this technique for measurements of individual carbon nanotubes, graphene, and other two-dimensional layered materials.

Bibliography

[1]   L. Shi, C. Dames, J. R. Lukes, P. Reddy, J. Duda, D. G. Cahill, J. Lee, A. Marconnet, K. E. Goodson, J.-H. Bahk, A. Shakouri, R. S. Prasher, J. Felts, W. P. King, B. Han, and J. C. Bischof, "Evaluating Broader Impacts of Nanoscale Thermal Transport Research," *Nanoscale Microscale Thermophys. Eng.*, vol. 19, no. August, pp. 127–165, 2015.

[2]   D. G. Cahill, K. Goodson, and A. Majumdar, "Thermometry and Thermal Transport in Micro/Nanoscale Solid-State Devices and Structures," *J. Heat Transfer*, vol. 124, no. 2, p. 223, 2002.

[3]   D. G. Cahill, "Analysis of heat flow in layered structures for time-domain thermoreflectance," *Rev. Sci. Instrum.*, vol. 75, no. 2004, pp. 5119–5122, 2004.

[4]   R. B. Wilson, B. a Apgar, L. W. Martin, and D. G. Cahill, "Thermoreflectance of metal transducers for optical pump-probe studies of thermal properties.," *Opt. Express*, vol. 20, no. 27, pp. 28829–38, 2012.

[5]   D.G. Cahill, H.E. Fischer, T. Klitsner, E.T. Swartz, and R.O. Pohl, "Thermal conductivity of thin films: Measurements and understanding.," *J. Vac. Sci. Technol*, vol 7, no. 3, pp. 1259–66, 1989

[6]   A.J. Schmidt, M. Chiesa, D.H. Torchinsky, J.A. Johnson, K.A. Nelson, and G. Chen, "Thermal conductivity of nanoparticle suspensions in insulating media measured with a transient optical grating and a hotwire.," *J. Appl. Phys.*, vol. 103, pp.083529, 2008

[7]   S. Shen, A. Henry, J. Tong, R. Zheng, and G. Chen, "Polyethylene nanofibres with very high thermal conductivities.," *Nat. Nanotechnol.*, vol. 5, no. 4, pp. 251–255, 2010.

[8]   Q. Li, C. Liu, X. Wang, and S. Fan, "Measuring the thermal conductivity of individual carbon nanotubes by the Raman shift method.," *Nanotechnology*, vol. 20, p. 145702, 2009.

[9]   Y. Yue, G. Eres, X. Wang, and L. Guo, "Characterization of thermal transport in micro/nanoscale wires by steady-state electro-Raman-thermal technique," *Appl. Phys. A Mater. Sci. Process.*, vol. 97, pp. 19–23, 2009.

[10]   I. K. Hsu, R. Kumar, A. Bushmaker, S. B. Cronin, M. T. Pettes, L. Shi, T. Brintlinger, M. S. Fuhrer, and J. Cumings, "Optical measurement of thermal transport in suspended carbon nanotubes," *Appl. Phys. Lett.*, vol. 92, no. 2008, pp. 2006–2009, 2008.

[11]   A. a Balandin, S. Ghosh, W. Bao, I. Calizo, D. Teweldebrhan, F. Miao, and C. N. Lau, "Superior thermal conductivity of single-layer graphene.," *Nano Lett.*, vol. 8, no. 3, pp. 902–7, Mar. 2008.

[12]   W. Cai, A. L. Moore, Y. Zhu, X. Li, S. Chen, L. Shi, and R. S. Ruoff, "Thermal transport in suspended and supported monolayer graphene grown by chemical vapor deposition.," *Nano Lett.*, vol. 10, no. 5, pp. 1645–51, May 2010.

[13]   C. Faugeras, B. Faugeras, M. Orlita, M. Potemski, R. R. Nair, and a. K. Geim, "Thermal conductivity of graphene in corbino membrane geometry," *ACS Nano*, vol. 4, no. 4, pp. 1889–1892, 2010.

[14]   A. Weathers and L. Shi, "Thermal Transport Measurement Techniques for Nanowires and Nanotubes," *Annu. Rev. Heat Transf.*, vol. 16, no. 1, pp. 101–134, 2013.

[15]   P. Kim, L. Shi, a Majumdar, and P. L. McEuen, "Thermal transport measurements of individual multiwalled nanotubes.," *Phys. Rev. Lett.*, vol. 87, p. 215502, 2001.

[16]   L. Shi, D. Li, C. Yu, W. Jang, D. Kim, Z. Yao, P. Kim, and A. Majumdar, "Measuring Thermal and Thermoelectric Properties of One-Dimensional Nanostructures Using a Microfabricated Device," *J. Heat Transfer*, vol. 125, no. October 2003, p. 881, 2003.

[17]   C. Yu, L. Shi, Z. Yao, D. Li, and A. Majumdar, "Thermal conductance and thermopower of an individual single-wall carbon nanotube.," *Nano Lett.*, vol. 5, no. 9, pp. 1842–6, Sep. 2005.

[18]   D. Li, Y. Wu, P. Kim, L. Shi, P. Yang, and A. Majumdar, "Thermal conductivity of individual silicon nanowires," *Appl. Phys. Lett.*, vol. 83, no. 2003, pp. 2934–2936, 2003.

[19]   H. Kim, I. Kim, H. J. Choi, and W. Kim, "Thermal conductivities of Si1-x Gex nanowires with different germanium concentrations and diameters," *Appl. Phys. Lett.*, vol. 96, no. 2010, pp. 2013–2016, 2010.

[20]   L. Yin, E. Kyung Lee, J. Woon Lee, D. Whang, B. Lyong Choi, and C. Yu, "The influence of phonon scatterings on the thermal conductivity of SiGe nanowires," *Appl. Phys. Lett.*, vol. 101, no. 2012, 2012.

[21]   M. T. Pettes, I. Jo, Z. Yao, and L. Shi, "Influence of polymeric residue on the thermal conductivity of suspended bilayer graphene.," *Nano Lett.*, vol. 11, no. 3, pp. 1195–200, Mar. 2011.

[22]   I. Jo, M. T. Pettes, E. Ou, W. Wu, and L. Shi, "Basal-plane thermal conductivity of few-layer molybdenum disulfide," *Appl. Phys. Lett.*, vol. 104, 2014.

[23]   J. Kim, E. Ou, D. P. Sellan, and L. Shi, "A four-probe thermal transport measurement method for nanostructures," *Rev. Sci. Instrum.*, vol. 86, no. 4, p. 044901, 2015.

[24]   A. F. Mills, *Heat Transfer*, 2nd ed. Boston: Irwin, 1992.

[25] J. Y. Murthy and S. R. Mathur, *Numerical Methods in Heat, Mass, and Momentum Transfer*. 2002.

[26] M. S. Dresselhaus, G. Dresselhaus, J. C. Charlier, and E. Hernández, "Electronic, thermal and mechanical properties of carbon nanotubes.," *Philos. Trans. A. Math. Phys. Eng. Sci.*, vol. 362, pp. 2065–2098, 2004.

[27] P. J. F. Harris, "Carbon nanotube composites," *Int. Mater. Rev.*, vol. 49, no. 1, pp. 31–43, 2004.

[28] J. N. Coleman, U. Khan, and Y. K. Gun'ko, "Mechanical reinforcement of polymers using carbon nanotubes," *Adv. Mater.*, vol. 18, no. 6, pp. 689–706, 2006.

[29] J. N. Coleman, U. Khan, W. J. Blau, and Y. K. Gun'ko, "Small but strong: A review of the mechanical properties of carbon nanotube-polymer composites," *Carbon N. Y.*, vol. 44, no. 9, pp. 1624–1652, 2006.

[30] Z. Spitalsky, D. Tasis, K. Papagelis, and C. Galiotis, "Carbon nanotube-polymer composites: Chemistry, processing, mechanical and electrical properties," *Prog. Polym. Sci.*, vol. 35, no. 3, pp. 357–401, 2010.

[31] C. L. Xu, B. Q. Wei, R. Z. Ma, J. Liang, X. K. Ma, and D. H. Wu, "Fabrication of aluminum / carbon nanotube composites and their electrical properties," *Carbon N. Y.*, vol. 37, no. 5, pp. 855–858, 1999.

[32] R. George, K. T. Kashyap, R. Rahul, and S. Yamdagni, "Strengthening in carbon nanotube/aluminium (CNT/Al) composites," *Scr. Mater.*, vol. 53, no. 10, pp. 1159–1163, 2005.

[33] J. Hone, M. C. Llaguno, M. J. Biercuk, a T. Johnson, B. Batlogg, Z. Benes, and J. E. Fischer, "Thermal properties of carbon nanotubes and nanotube-based materials," *Appl. Phys. A Mater. Sci. Process.*, vol. 74, no. 3, pp. 339–343, 2002.

[34] E. Pop, D. Mann, Q. Wang, K. Goodson, and H. Dai, "Thermal Conductance of an Individual Single-Wall Carbon Nanotube above Room Temperature," *Nano Lett.*, vol. 6, pp. 96–100, 2005.

[35] M. Fujii, X. Zhang, H. Xie, H. Ago, K. Takahashi, T. Ikuta, H. Abe, and T. Shimizu, "Measuring the thermal conductivity of a single carbon nanotube," *Phys. Rev. Lett.*, vol. 95, no. 6, pp. 8–11, 2005.

[36] M. J. Biercuk, M. C. Llaguno, M. Radosavljevic, J. K. Hyun, a. T. Johnson, and J. E. Fischer, "Carbon nanotube composites for thermal management," *Appl. Phys. Lett.*, vol. 80, no. 2002, pp. 2767–2769, 2002.

[37] H. Huang, C. Liu, Y. Wu, and S. Fan, "Aligned carbon nanotube composite films for thermal management," *Adv. Mater.*, vol. 17, no. 13, pp. 1652–1656, 2005.

[38]   J. Xu and T. S. Fisher, "Enhancement of thermal interface materials with carbon nanotube arrays," *Int. J. Heat Mass Transf.*, vol. 49, no. 9–10, pp. 1658–1666, 2006.

[39]   M. T. Pettes, M. M. Sadeghi, H. Ji, I. Jo, W. Wu, R. S. Ruoff, and L. Shi, "Scattering of phonons by high-concentration isotopic impurities in ultrathin graphite," *Phys. Rev. B*, vol. 91, pp. 1–13, 2015.